Itinerant quantum critical point with fermion pockets and hotspots

Zi Hong Liu[a,b], Gaopei Pan[a,b], Xiao Yan Xu[c], Kai Sun[d], and Zi Yang Meng[e,a,f,g,h,1]

[a]Beijing National Laboratory for Condensed Matter Physics and Institute of Physics, Chinese Academy of Sciences, Beijing 100190, China; [b]School of Physical Sciences, University of Chinese Academy of Sciences, Beijing 100190, China; [c]Department of Physics, Hong Kong University of Science and Technology, Hong Kong, China; [d]Department of Physics, University of Michigan, Ann Arbor, MI 48109; [e]Department of Physics, The University of Hong Kong, Hong Kong, China; [f]Chinese Academy of Sciences Center of Excellence in Topological Quantum Computation, University of Chinese Academy of Sciences, Beijing 100190, China; [g]School of Physical Sciences, University of Chinese Academy of Sciences, Beijing 100190, China; and [h]Songshan Lake Materials Laboratory, Dongguan, Guangdong 523808, China

Edited by Subir Sachdev, Harvard University, Cambridge, MA, and approved July 1, 2019 (received for review January 31, 2019)

Metallic quantum criticality is among the central themes in the understanding of correlated electronic systems, and converging results between analytical and numerical approaches are still under review. In this work, we develop a state-of-the-art large-scale quantum Monte Carlo simulation technique and systematically investigate the itinerant quantum critical point on a 2D square lattice with antiferromagnetic spin fluctuations at wavevector $\mathbf{Q} = (\pi, \pi)$—a problem that resembles the Fermi surface setup and low-energy antiferromagnetic fluctuations in high-Tc cuprates and other critical metals, which might be relevant to their non–Fermi-liquid behaviors. System sizes of $60 \times 60 \times 320$ ($L \times L \times L_\tau$) are comfortably accessed, and the quantum critical scaling behaviors are revealed with unprecedented high precision. We found that the antiferromagnetic spin fluctuations introduce effective interactions among fermions and the fermions in return render the bare bosonic critical point into a different universality, different from both the bare Ising universality class and the Hertz–Mills–Moriya RPA prediction. At the quantum critical point, a finite anomalous dimension $\eta \sim 0.125$ is observed in the bosonic propagator, and fermions at hotspots evolve into a non-Fermi liquid. In the antiferromagnetically ordered metallic phase, fermion pockets are observed as the energy gap opens up at the hotspots. These results bridge the recent theoretical and numerical developments in metallic quantum criticality and can serve as the stepping stone toward final understanding of the 2D correlated fermions interacting with gapless critical excitations.

quantum phase transition | non-Fermi liquid | critical exponent

In the study of correlated materials, quantum criticality in itinerant electron systems is of great importance and interest (1–8). It plays a vital role in the understanding of anomalous transport, strange metal, and non–Fermi-liquid behaviors (9–13) in heavy-fermion materials (14, 15), Cu- and Fe-based high-temperature superconductors (16–18) as well as the recently discovered pressure-driven quantum critical point (QCP) between magnetic order and superconductivity in transition-metal monopnictides, CrAs (19), MnP (20), $\mathrm{CrAs}_{1-x}\mathrm{P}_x$ (21), and other Cr/Mn-3d electron systems (22). However, despite extensive efforts in recent decades (1–9, 23–30), itinerant quantum criticality is still among the most challenging subjects in condensed matter physics, due to its nonperturbative nature, and many important questions and puzzles remain open.

The recent development of sign-problem-free quantum Monte Carlo techniques has paved an additional pathway toward sharpening our understanding about this challenging problem (see a concise commentary in ref. 31 and a review in ref. 32 that summarize the recent progress). Via coupling a Fermi liquid with various bosonic critical fluctuations, a wide variety of itinerant quantum critical systems have been studied, such as Ising-nematic (33, 34), ferromagnetic (13), charge density wave (35), spin density wave (36–41), and interaction-driven topological phase transitions and gauge fields (42–47). With the fast development of quantum Monte Carlo (QMC) techniques, in particular the self-learning Monte Carlo (SLMC) (48–54) and elective momentum ultrasize quantum Monte Carlo (EQMC) (41), it now becomes possible to explore larger system sizes than those handled with conventional determinantal quantum Monte Carlo, consequently allowing us to access the genuine scaling behaviors in the infrared (IR) limit for itinerant quantum criticality.

Although many intriguing results and insights have been obtained, for the search of novel quantum critical points beyond the Hertz–Millis–Moriya theory, a major gap between theory and numerical studies still remains. So far, in QMC simulations, among all recently studied itinerant QCPs, either the Hertz–Millis mean-field scaling behavior is found (33, 40) or unpredicted exponents, deviating from existing theories, are observed (13), while theoretically proposed properties beyond the Hertz–Millis–Moriya scaling behaviors still remain to be numerically observed and verified.

In this paper, we aim at improving the convergence between theoretical and numerical studies by focusing on itinerant QCPs with finite ordering wavevector $\mathbf{Q} \neq 0$, e.g., charge/spin density waves (CDW/SDW). One key question in the study of these

PHYSICS

Significance

The present work summarizes major progress in research on the itinerant quantum critical point (QCP). The authors designed a model and developed quantum Monte Carlo simulation to examine itinerant QCPs generated by antiferromagnetic fluctuations. The model has immediate relevance to a wide range of strongly correlated systems, such as cuprate superconductors. Large system size and low temperature are comfortably accessed and quantum critical scaling relations are revealed with high accuracy. At the QCP, a finite anomalous dimension is observed, and fermions at hotspots evolve into a non-Fermi liquid. These results are being observed in an unbiased manner and they could bridge future developments both in analytical theory and in numerical simulation of itinerant QCPs.

Author contributions: X.Y.X., K.S., and Z.Y.M. designed research; Z.H.L., G.P., X.Y.X., K.S., and Z.Y.M. performed research; X.Y.X., K.S., and Z.Y.M. analyzed data; and K.S. and Z.Y.M. wrote the paper.

The authors declare no conflict of interest.

This article is a PNAS Direct Submission.

[1]To whom correspondence may be addressed. Email: zymeng@hku.hk.

This article contains supporting information online at www.pnas.org/lookup/suppl/doi:10.1073/pnas.1901751116/-/DCSupplemental.

QCPs is about the universality class, i.e., whether all these types of QCPs, e.g., commensurate and incommensurate CDW/SDW QCPs, belong to the same universality class or not. To the leading order, within the random phase approximation (RPA), as long as the ordering wavevector $\mathbf{Q}$ is smaller than twice the Fermi wavevector $2k_F$ or, more precisely, as we shift the Fermi surface (FS) by the ordering wavevector $\mathbf{Q}$ in the momentum space, the shifted FS and the original one shall cross at hotspots, instead of tangentially touching with or overrunning each other, and the same (linear ω) Landau damping and critical dynamics are predicated regardless of microscopic details, implying the dynamic critical exponent $z = 2$. For a 2D system, this makes the effective dimensions $d + z = 4$, coinciding with the upper critical dimension. As a result, within the Hertz–Millis approximation, mean-field critical exponents shall always be expected, up to possible logarithmic corrections, and thus all these QCPs belong to the same universality class (1–3, 55).

On the other hand, more recent theoretical developments point out that this conclusion becomes questionable once higher-order effects are taken into account. In particular, 2 different universality classes need to be distinguished, depending on whether $2\mathbf{Q}$ coincides with a lattice vector or not, which are dubbed as $2\mathbf{Q} = \Gamma$ and $2\mathbf{Q} \neq \Gamma$ to demonstrate that $2\mathbf{Q}$, mod a reciprocal lattice vector, coincides or not with the Γ point. Among these 2 cases, $2\mathbf{Q} = \Gamma$ (e.g., antiferromagnetic QCP with $\mathbf{Q} = (\pi, \pi)$) is highly exotic. As Abanov *et al.* (23) pointed out explicitly, in this case the Hertz–Millis mean-field scaling law breaks down and a non-zero anomalous dimension emerges. In addition, the critical fluctuations will also change the fermion dispersion near the hotspots, resulting in a critical-fluctuation–induced Fermi surface nesting: i.e., even if one starts from a Fermi surface without nesting, the renormalization group (RG) flow of the Fermi velocity will deform the Fermi surface at hotspots toward nesting (23). This Fermi surface deformation will further increase the anomalous dimension and make the scaling exponent deviate even farther from Hertz–Millis prediction (23, 24), and even modifies the dynamic critical exponent z, as pointed out explicitly by Metlitski and Sachdev (26) and others (28, 29). For $2\mathbf{Q} \neq \Gamma$, on the other hand, these exotic behaviors are not expected, at least up to the same order in the $1/N$ expansion, and thus presumably they follow the Hertz–Millis mean-field scaling relation.

On the numerical side, a QCP with $2\mathbf{Q} \neq \Gamma$ was recently studied (40, 41) and the results are in good agreement with the Hertz–Millis–Moriya theory. For the more exotic case with $2\mathbf{Q} = \Gamma$, the numerical result is less clear because in QMC simulations, a superconducting dome usually arises and covers the QCP (38, 39, 56). Outside the superconducting dome, at some distance away from the QCP, mean-field exponents are observed to be consistent with the Hertz–Millis–Moriya theory. However, whether the predicted anomalous (non–mean-field) behaviors (23, 26, 28, 29) will arise in the close vicinity of the QCP remains an open question, which requires the suppression of the superconducting order. In addition, due to the divergent length scale at a QCP, to obtain reliable scaling exponents, large system sizes are necessary to overcome the finite-size effect.

In this paper, we perform large-scale quantum Monte Carlo simulations to study the antiferromagnetic metallic quantum critical point (AFM-QCP) with $2\mathbf{Q} = \Gamma$. In this study, 2 main efforts are made to accurately obtain the critical behavior in the close vicinity of the QCP. 1) We design a lattice model that realizes the desired AFM-QCP with the superconducting dome greatly suppressed to expose the quantum critical regions and 2) we use the determinantal quantum Monte Carlo (DQMC) as well as the EQMC, both with self-learning updates to access much larger system sizes beyond existing efforts. The more conventional DQMC technique allow us to access system sizes up to $28 \times 28 \times 200$ for $L \times L \times L_\tau$ for a 2D square lattice, while EQMC can access much larger sizes ($60 \times 60 \times 320$) to further reduce the finite-size effect and confirms scaling exponents with higher accuracy. These 2 efforts (1 and 2) allow us to access the metallic quantum critical region and to reveal its IR scaling behaviors with great precision, where we found a large anomalous dimension significantly different from the Hertz–Millis theory prediction, and we also observed that the Fermi surface near the hotspots rotates toward nesting at the QCP, as predicted in

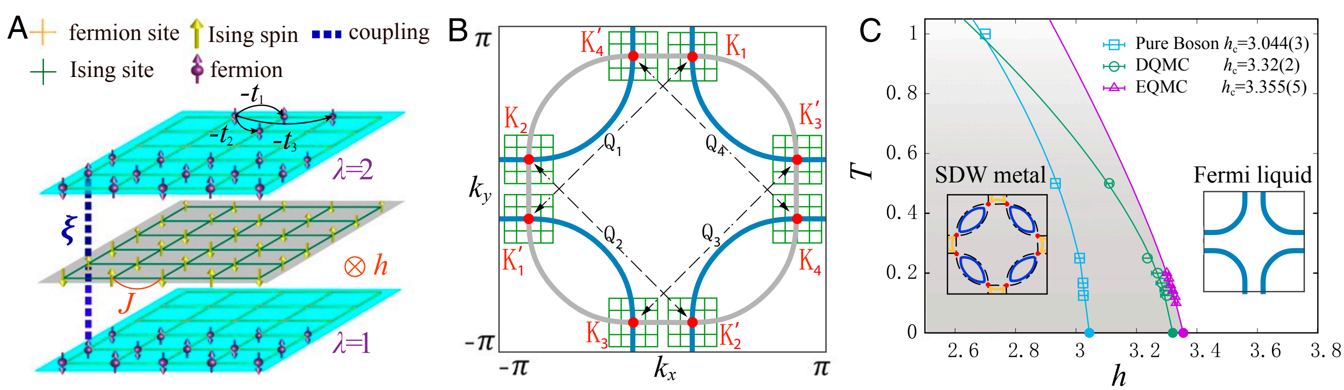

Fig. 1. (*A*) Illustration of the model in Eq. **1**. Fermions reside on 2 of the layers ($\lambda = 1,2$) with intralayer nearest-, second-, and third-neighbor hoppings t_1, t_2, and t_3. The middle layer is composed of Ising spins s_i^z, subject to nearest-neighbor antiferromagnetic Ising coupling J and a transverse magnetic field h. Between the layers, an on-site Ising coupling is introduced between fermion and Ising spins (ξ). (*B*) Brillouin zone (BZ) of the model in Eq. **1**. The blue lines are the FS of H_f and $\mathbf{Q}_i = (\pm\pi, \pm\pi)$, $i = 1, 2, 3, 4$ are the AFM wavevectors, and the 4 pairs of $\{\mathbf{K}_i, \mathbf{K}_i'\}$, $i = 1, 2, 3, 4$ are the position of the hotspots (red circles), where each pair is connected by a $\mathbf{Q}_i$ vector. The folded FS (gray lines) comes from translating the bare FS by momentum $\mathbf{Q}_i$. The green patches show the $\mathbf{k}$ mesh built around hotspots, and the number of momentum points inside each patch is denoted as N_f. (*C*) Phase diagram of model Eq. **1**. The light blue line marks the phase boundaries of the pure bosonic model H_b, with a QCP (light blue circle) at $h_c = 3.044(3)$ (57, 58) with 3D Ising universality. After coupling with fermions, the QCP shifts to higher values. The green solid circle is the QCP obtained with DQMC ($h_c = 3.32(2)$). The violet solid circle is the QCP obtained from EQMC ($h_c = 3.355(5)$); although the position of the QCP shifts, as it is a nonuniversal quantity, the scaling behavior inside the quantum critical region is consistent between DQMC and EQMC. The EQMC scheme can comfortably capture the IR physics of AFM-QCP, with much larger system sizes, $60 \times 60 \times 320$, compared with those in DQMC with $28 \times 28 \times 200$. The procedure of how the phase boundary is determined is shown in *SI Appendix, Thermal Phase Transition*.

the RG analysis (23, 26, 28, 29). And quantitative comparison between theory and numerical results is also performed. These results bridge the recent theoretical and numerical developments and are the precious stepping stone toward final understanding of the metallic quantum criticality in 2D.

Model and Method

Antiferromagnetic Fermiology. The square lattice AFM model that we designed is schematically shown in Fig. 1*A* with 2 fermion layers and 1 Ising spin layer in between. Fermions are subject to intralayer nearest-, second-, and third-neighbor hoppings t_1, t_2, and t_3, as well as the chemical potential μ. The Ising spin layer is composed of Ising spins s_i^z with nearest-neighbor antiferromagnetic coupling J $(J>0)$ and a transverse magnetic field h along s^x. Fermions and Ising spins are coupled together via an interlayer on-site Ising coupling ξ. The Hamiltonian is given as

$$H = H_f + H_b + H_{fb}, \qquad [1]$$

where

$$H_f = -t_1 \sum_{\langle ij\rangle,\lambda,\sigma} c^\dagger_{i,\lambda,\sigma} c_{j,\lambda,\sigma} - t_2 \sum_{\langle\langle ij\rangle\rangle,\lambda,\sigma} c^\dagger_{i,\lambda,\sigma} c_{j,\lambda,\sigma} - t_3 \sum_{\langle\langle\langle ij\rangle\rangle\rangle,\lambda,\sigma} c^\dagger_{i,\lambda,\sigma} c_{j,\lambda,\sigma} + h.c. - \mu \sum_{i,\lambda,\sigma} n_{i,\lambda,\sigma} \qquad [2]$$

$$H_b = J \sum_{\langle ij\rangle} s_i^z s_j^z - h \sum_i s_i^x \qquad [3]$$

$$H_{fb} = -\xi \sum_i s_i^z \left(\sigma^z_{i,1} + \sigma^z_{i,2}\right), \qquad [4]$$

and $\sigma^z_{i,\lambda} = \frac{1}{2}(c^\dagger_{i,\lambda,\uparrow} c_{i,\lambda,\uparrow} - c^\dagger_{i,\lambda,\downarrow} c_{i,\lambda,\downarrow})$ is the fermion spin along z.

H_b describes a 2D transverse-field Ising model and has a phase diagram spanning along the axes of temperature T and h. As shown in Fig. 1*C* (light blue line), at $h=0$, the system undergoes a 2D Ising thermal transition at a finite T. Gradually turning on a finite h, the system experiences the same AFM 2D Ising transition with a lower transition temperature, until $h=h_c$ (3.04438(2)), where the transition turns into a $T=0$ quantum phase transition in the 3D Ising universality class (57, 58). Such an antiferromagnetic order has a wavevector $\mathbf{Q}=(\pi,\pi)$, as denoted by the $\mathbf{Q}_i$ with $i=1,2,3,4$ in Fig. 1*B*.

The fermions in H_f experience the AFM fluctuations in H_b via the fermion-spin coupling H_{fb}. As shown in Fig. 1*B*, the original FS and FSs from zone folding (shifted by the ordering wavevector $\mathbf{Q}_i$ $(i=1,2,3,4)$) form Fermi pockets and the so-called hotspots, which are crossing points between the original and the folded FSs labeled as $\mathbf{K}_i$ and $\mathbf{K}_i'$ with $i=1,2,3,4$.

In the simulation, we set $t_1=1.0$, $t_2=-0.32$, $t_3=0.128$, $J=1$, $\mu=-1.11856$ (electron density $\langle n_{i,\lambda}\rangle \sim 0.8$), the coupling strength $\xi=1.0$, and leave h as control parameters. The parameters are chosen according to ref. 59, such that deep in the AFM phase of Ising spins, the FS exhibits 4 big Fermi pockets and 4 pairs of hotspots (hotspot number $N_{h.s.}=8\times 2=16$ where the factor 2 comes from 2 fermion layers) as a result of band folding due to AFM ordering. Such an antiferromagnetic fermiology is summarized in Fig. 1*B*.

Ising Scaling for the Bare Boson Model. Before presenting our results about the itinerant AFM-QCP, we first discuss the QCP in the pure boson limit without fermions, which serves as a benchmark for the nontrivial itinerant quantum criticality. It is known that the pure boson QCP (H_b) belongs to the $(2+1)$D Ising universality class (13, 57, 58). This can be demonstrated numerically by calculating the dynamic spin susceptibility

$$\chi(T,h,\vec{q},\omega_n) = \frac{1}{L^2}\sum_{ij}\int_0^\beta d\tau\, e^{i\omega_n\tau - i\vec{q}\cdot\vec{r}_{ij}} \langle s_i^z(\tau) s_j^z(0)\rangle. \qquad [5]$$

In principle, near the QCP, the functional form of the dynamic spin susceptibility is complicated and hard to write explicitly. However, in the quantum critical region, as we set $h=h_c$, the scaling functional form of $\chi(T,h_c,\vec{q},\omega_n)$ can be described by the asymptotic form

$$\chi(T,h_c,\mathbf{q},\omega_n) = \frac{1}{c_t T^2 + (c_q|\mathbf{q}|^2 + c_\omega \omega^2)^{a_q/2}}, \qquad [6]$$

where $a_q = 2-\eta = 1.964(2)$ is the universal critical exponent of the 3D Ising universal class, and c_t, c_q, and c_ω are nonuniversal coefficients. This scaling form Eq. **6** explicitly respects the emergent Lorentz symmetry at the Ising critical point.

Without fermions, we can use the standard path-integral scheme to map the 2D transverse-field Ising model to a $(2+1)$D classical Ising model (60). To solve this anisotropic 3D Ising model with Monte Carlo simulations, we performed Wolff (61) and Swendsen–Wang (62) cluster updates to access sufficiently large system sizes and low temperature. The dynamic susceptibilities are shown in Fig. 2. To explore the momentum

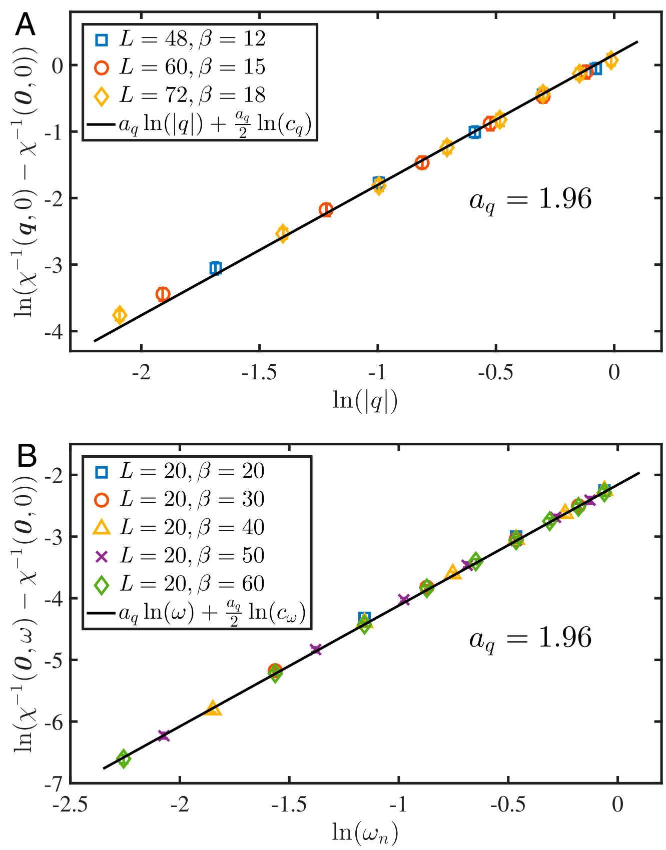

Fig. 2. (*A*) Momentum dependence of the $\chi(\mathbf{q},\omega=0)$ at $h=h_c$, for the bare boson model H_b. The system sizes are $L=48, 60, 72$, respectively, and to achieve quantum critical scaling, $\beta \propto L$ is applied. The line going through the data points is $a_q \ln(|q|) + \frac{a_q}{2}\ln(c_q)$, with $a_q = 2-\eta = 1.96$. (*B*) Frequency dependence of $\chi(\mathbf{q}=\mathbf{0},\omega)$ at $h=h_c$, for the bare boson model H_b. The system size is $L=20$ with increasing $\beta = 20, 30, 40, 50$, and 60. The line going through the data points is $a_q \ln(\omega) + \frac{a_q}{2}\ln(c_\omega)$, with $a_q = 2-\eta = 1.96$.

PHYSICS

dependence of the susceptibility, we plot $\chi^{-1}(T, h_c, \mathbf{q}, \omega=0) - \chi^{-1}(T, h_c, \mathbf{q}=0, \omega=0)$, where the momentum $\mathbf{q}$ is measured from $\mathbf{Q}=(\pi,\pi)$ and the substraction is to get rid of the finite-temperature background, such that the following scaling relation is expected at low T:

$$\chi^{-1}(T, h_c, \mathbf{q}, \omega=0) - \chi^{-1}(T, h_c, \mathbf{q}=0, \omega=0) = c_q^{a_q/2}|\mathbf{q}|^{a_q}. \quad [7]$$

As shown in Fig. 2*A* such a scaling relation is indeed observed with $L=48, 60$, and 72 with $\beta=1/T \propto L$. The power-law divergence of the $(2+1)$D Ising quantum critical susceptibility with power $a_q=2-\eta=1.96$ is clearly revealed (the 3D Ising anomalous dimension $\eta=0.04$).

A similar scaling relation is also observed in the frequency dependence as shown in Fig. 2*B*, where we plot

$$\chi^{-1}(T, h_c, 0, \omega) - \chi^{-1}(T, h_c, 0, \omega=0) = c_\omega^{a_q/2}\omega^{a_q} \quad [8]$$

for $L=20$ with increasing β. The expected power-law decay with the small anomalous dimension $a_q=2-\eta=1.96$ is clearly obtained. Hence, the data in Fig. 2 *A* and *B* confirm the QCP for the pure boson part H_b in Eq. **1** belongs to the $(2+1)$D Ising universality class.

DQMC and EQMC. To solve the problem in Eq. **1** we use 2 complementary fermionic quantum Monte Carlo schemes.

The first one is the standard DQMC (13, 63–65) with the SLMC update scheme (48–54) to speed up the simulation. In SLMC, we first perform the standard DQMC simulation on the model in Eq. **1** and then train an effective boson Hamiltonian that contains long-range 2-body interactions both in spatial and in temporal directions. The effective Hamiltonian serves as the proper low-energy description of the problem at hand with the fermion degree of freedom integrated out. We then use the effective Hamiltonian to guide the Monte Carlo simulations; i.e., we perform many sweeps of the effective bosonic model (as the computational cost of updating the boson model is $O(\beta N)$, dramatically lower than the update of the fermion determinant which scales as $O(\beta N^3)$) and then evaluate the fermion determinant of the original model in Eq. **1** such that the detailed balance of the global update is satisfied. As shown in our previous works (40, 49, 50, 53, 54), the SLMC can greatly reduce the autocorrelation time in the conventional DQMC simulation and make the larger systems and lower temperature accessible.

The other method is the EQMC (41). EQMC is inspired by the awareness that critical fluctuations mainly couple to fermions near the hotspots. Thus, instead of including all of the fermion degrees of freedom, we ignore fermions far away from the hotspots and focus only on momentum points near the hotspots in the simulation. This approximation will produce different results for nonuniversal quantities compared with the original model, such as h_c or critical temperature. However, for universal quantities, such as scaling exponents, which are independent of microscopic details and the high energy cutoff, EQMC has been shown to generate values consistent with those obtained from standard DQMC (41).

In EQMC, because a local coupling (in real space) becomes nonlocal in the momentum basis, one can no longer use the local update as in standard DQMC, as that would cost $\beta N \cdot O(\beta N_f^3)$ computational complexity. Fortunately, cumulative update schemes in the SLMC have been developed recently (49, 50). Such a cumulative update is a global move of the Ising spins and gives rise to the complexity $O(\beta N_f^3)$ for computing the fermion determinant. Since N_f can be much smaller than N, speedup of the order $(\frac{N}{N_f})^3 \sim 10^3$ of EQMC over DQMC, with $\frac{N}{N_f} \sim 10$, can be easily achieved.

In the square lattice model, as shown in Fig. 1*B*, the AFM wavevectors $\mathbf{Q}_i$ connect 4 pairs of hotspots ($N_{h.s.}=8$ in 1 layer and $N_{h.s.}=16$ in 2 layers). In the IR limit, only fluctuations connecting each pair of hotspots are important to the universal scaling behavior in the vicinity of the QCP (7, 9, 23–26, 66). Hence, to study this universal behavior, we draw 1 patch around each $\mathbf{K}_l$ and keep fermion modes therein and neglect other parts of the BZ. In this way, instead of the original $N=L\times L$ momentum points, EQMC keeps only $N_f=L_f\times L_f$ momentum points for fermions inside each patch. Here, L and L_f denote the linear size of the original lattice and the size of the patch, respectively.

DQMC and EQMC are complementary to each other; the former provides unbiased results with relatively small systems and the latter, as an approximation, provides results closer to the QCP with finite-size effects better suppressed. One other benefit of EQMC is that it provides much higher momentum resolution close to the hotspots. Fig. 3 depicts the FS of the model in Eq. **1** obtained from $G(\mathbf{k},\beta/2)\sim A(\mathbf{k},\omega=0)$ via DQMC (Fig. 3 *A* and *B*) and EQMC (Fig. 3 *C* and *D*). Fig. 3 *A* and *C* is for $h<h_c$, i.e., inside the AFM metallic phase, whereas Fig. 3 *B* and *D* is for $h\sim h_c$, i.e., at the AFM-QCP. The DQMC data are obtained from $L=28$, $\beta=14$ simulations, and it is clear that the momentum resolution is still too low to provide detailed FS structures near the hotspots. With EQMC, the system sizes are $L=60$ and $\beta=14$ in Fig. 3 *C* and *D*, and the momentum resolution is dramatically improved. For example, in Fig. 3*C*, inside the AFM metallic phase, the gap at hotspots is clearly visualized. And in Fig. 3*D*, at the AFM-QCP the FS recovers the shape of the noninteracting one, and non–Fermi-liquid behavior emerges at the hotspots as shown in the next section. To capture these important physics, EQMC and its higher-momentum resolution play a vital role.

Results

Non-Fermi Liquid. As we emphasized above, the dramatically improved momentum resolution in EQMC enables us to study

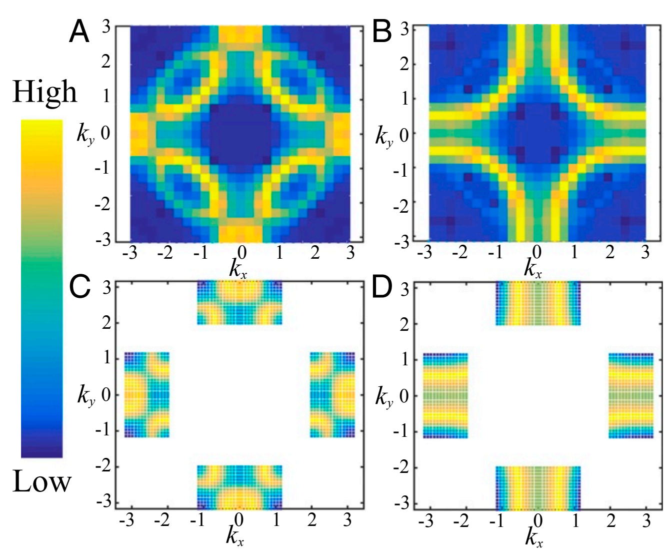

Fig. 3. (*A–D*) Fermi surface obtained from DQMC (*A* and *B*) and EQMC (*C* and *D*). Here we show the Fermi surface by plotting the fermion spectrum function at 0 energy $A(\mathbf{k},\omega=0)$ using the standard approximation $G(\mathbf{k},\beta/2)\sim A(\mathbf{k},\omega=0)$. (*A* and *C*) FS in the AFM ordered phase ($h<h_c$), where Fermi pockets are formed from zone folding. DQMC and EQMC results are consistent with each other, while EQMC (with system size $L=60$) gives much higher resolution in comparison with DQMC ($L=28$). (*B* and *D*) Similar comparison at the QCP ($h=h_c$).

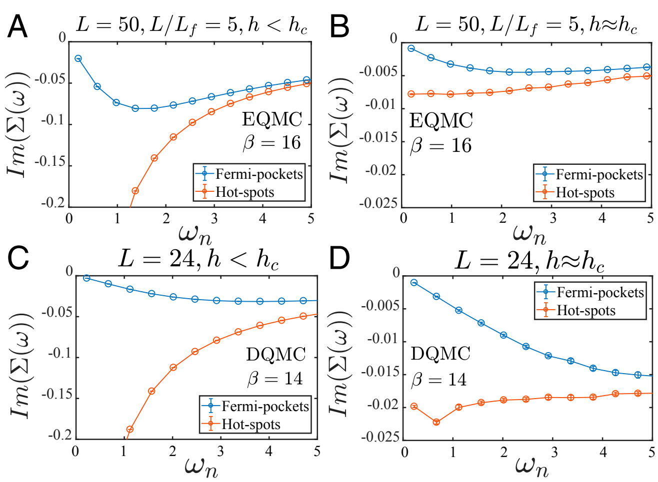

Fig. 4. (*A*) Self-energy obtained from EQMC inside the AFM-metal phase ($h < h_c$). On the Fermi pockets, the system is in a Fermi-liquid state as shown by the linearly vanishing $\mathrm{Im}(\Sigma(\mathbf{k}, \omega))$ at small ω. At the hotspot, due to the Fermi surface reconstruction, an energy gap opens up, resulting in a divergent $\mathrm{Im}(\Sigma(\mathbf{k}, \omega))$. (*B*) Self-energy obtained from EQMC at the AFM-QCP ($h \sim h_c$). On the Fermi pockets, the system remains a Fermi liquid as shown by the linearly vanishing $\mathrm{Im}(\Sigma(\mathbf{k}, \omega))$ at small ω. At the hotspot, $\mathrm{Im}(\Sigma(\mathbf{k}, \omega))$ has a small but finite value as ω goes to 0, which is the signature of a non-Fermi liquid. *C* and *D* show the same quantities produced in DQMC simulations with smaller system sizes, where qualitative behaviors remain the same.

the fermionic modes on the FS more precisely. We studied the fermion self-energies in the AFM-metal phase and at the AFM-QCP. The results are shown in Fig. 4.

In the AFM-metal phase, although the bands are folded according to Fig. 1*B*, the system remains a Fermi liquid, with a band gap opening up at hotspots. Such expectations are revealed in Fig. 4 *A* and *C*. The Matsubara-frequency dependence of the $\mathrm{Im}(\Sigma(\mathbf{k}, \omega))$ either goes to 0 linearly (on the pockets) or diverges (at the hotspot). Near the AFM-QCP, however, the situation is very different. Fermions at the hotspots show non–Fermi-liquid behavior; namely, as shown in Fig. 4 *B* and *D*, $\mathrm{Im}(\Sigma(\mathbf{k}, \omega))$ goes to a small constant at low ω, and no sign of either vanishing or diverging is observed. The fermions away from the hotspots remain Fermi liquid-like. Once again, DQMC and EQMC simulations give consistent results with the same qualitative behavior.

It is worthwhile to point out that, at the QCP, for fermions at the hotspot, a finite imaginary part in fermion self-energy is observed, which does not seem to decay to 0 as we reduce the frequency. This behavior (a constant term in the imaginary part of the self-energy) is not yet theoretically understood. However, it is consistent with similar QMC studies, where such a finite or constant term always seems to emerge near itinerant QCPs (13, 40, 41).

Universality Class and Critical Exponents. In our previous work on triangle lattice AFM-QCP (40) with $2\mathbf{Q} \neq \Gamma$ (in fact in that case one has $3\mathbf{Q} = \Gamma$), the bosonic susceptibilities $\chi(T, h_c, \boldsymbol{q}, \omega)$ (defined in Eqs. **5** and **6**) close to the QCP, revealed with $30 \times 30 \times 600$ ($L \times L \times L_\tau$) from DQMC, fit to the form of

$$\chi(T, h_c, \mathbf{q}, \omega_n) = \frac{1}{(c_t T + c_t' T^2) + c_q|\mathbf{q}|^2 + c_\omega \omega + c_\omega' \omega^2}. \quad [9]$$

In particular, at low ω, $\chi^{-1}(0, h_c, 0, \omega)$ exhibits a crossover behavior from ω^2 to ω and the susceptibility scales with $\mathbf{q}$ as $\chi^{-1}(0, h_c, \mathbf{q}, 0) \propto |\mathbf{q}|^2$; i.e., no anomalous dimension is observed. The system acquires a dynamic critical exponent $z = 2$, consistent with the Hertz–Millis mean-field expectation of the AFM-QCP at its upper critical dimension $d + z = 4$.

For the square lattice model in this paper, we expect that the dynamic spin susceptibility has the following asymptotic form in the quantum critical region ($h = h_c$):

$$\chi(T, h_c, \mathbf{q}, \omega_n) = \frac{1}{c_t T^{a_t} + (c_q|\mathbf{q}|^2 + c_\omega \omega)^{1-\eta} + c_\omega' \omega^2}. \quad [10]$$

This functional form is similar to the Hertz–Millis theory, but we allow an anomalous dimension (η) as a free fitting parameter. We used this functional form to guide our data analysis.

We first look at the $\mathbf{q}$ dependence of χ^{-1}; as shown in Fig. 5*A*, the momentum $|\mathbf{q}|$ is measured with respect to the hotspot $\mathbf{K}$. Here we plot the susceptibility data by substracting the finite-temperature background as $\chi^{-1}(T, h_c, |\mathbf{q}|, 0) - \chi^{-1}(T, h_c, 0, 0) = c_q|\mathbf{q}|^{a_q}$, where $a_q = 2(1-\eta)$, and fit the curve to obtain the coefficient c_q and the anomalous dimension η, as shown by the solid line in Fig. 5*A*. Using EQMC, with the system size as large as $L = 60$, the power-law behavior $\chi^{-1}(|\mathbf{q}|) \propto |\mathbf{q}|^{a_q}$ clearly manifests, with $c_q = 1.04(1)$ and $a_q = 2(1-\eta) = 1.75(2)$ with $\eta = 0.125$. In DQMC simulation, we observed the same exponents $\eta = 0.11(2)$, with slightly lower accuracy due to smaller system sizes; the DQMC results are shown in

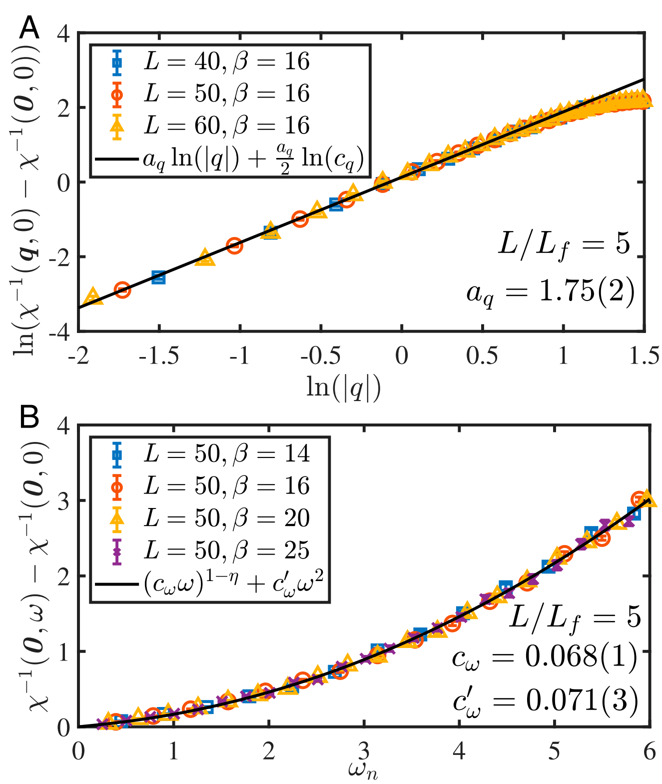

Fig. 5. (*A*) $|\mathbf{q}|$ dependence of the bosonic susceptibilities $\chi(T=0, h=h_c, \mathbf{q}, \omega=0)$ at the AFM-QCP. The system sizes are $L = 40$, 50, and 60. The fitting line according to the form in Eq. **10** reveals that there is an anomalous dimension in $\chi^{-1}(\mathbf{q}) \sim |\mathbf{q}|^{2(1-\eta)}$ with $\eta = 0.125$. (*B*) ω dependence of the bosonic susceptibilities $\chi(T=0, h=h_c, \mathbf{q}=0, \omega)$ at the AFM-QCP. The system size is $L = 50$ and the temperature is as low as $\beta = 25$ ($L_\tau = 500$). The fitting line according to the form in Eq. **10** reveals that there is an anomalous dimension in $\chi^{-1}(\omega) \sim \omega^{(1-\eta)}$ at small ω and crossover to $\chi^{-1}(\omega) \sim \omega^2$ at high ω.

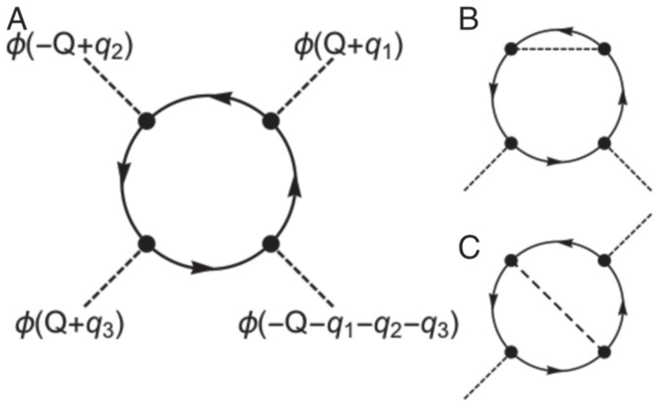

Fig. 6. (*A*) Feynman diagram representing a 4-boson interaction vertex. Dashed lines, $\phi(\mathbf{k})$, represent spin fluctuations at momentum **k** and we set $q << Q$. Because low-energy physics are dominated by fermionic excitations near the FS, 2 of the 4 boson legs must have momenta near **Q**, while the other 2 are near $-\mathbf{Q}$ to keep the fermions near the FS as shown. For $2\mathbf{Q}=\Gamma$, $+\mathbf{Q}$ and $-\mathbf{Q}$ become identical, and thus there exist 2 ways to contract the external legs as shown in *B* and *C*. For $2\mathbf{Q}\neq\Gamma$, however, only the contraction shown in *B* is allowed, while the momentum conservation law is violated in *C*.

SI Appendix, *Comparison of EQMC and DQMC at Quantum Critical Region*.

For the frequency dependence in χ, as shown in Fig. 5*B*, we analyze the $\chi^{-1}(T,h_c,0,\omega)-\chi^{-1}(T,h_c,0,0)$ to subtract the finite-temperature background and test the predicted anomalous dimension $\eta=0.125$ in Eq. **10** and the data points fit very well the expected functional form

$$\chi^{-1}(\omega)=(c_\omega\omega)^{1-\eta}+c'_\omega\omega^2, \qquad \textbf{[11]}$$

where we obtained the values of the coefficients $c_\omega=0.068(1)$ and $c'_\omega=0.071(3)$. It is worthwhile to note that the crossover behavior in $\chi^{-1}(\omega)$ is very interesting, since at low frequency, the anomalous dimension in $\omega^{0.875}$ dominates bosonic susceptibility and this means that the coupling of the fermions with the critical bosons has changed the universality behavior from the bare $(2+1)$D Ising universality with $\eta=0.036$ to a new one of AFM-QCP with $\eta=0.125$. However, at high frequency, where the coupling between fermions and bosons becomes irrelevant, the bare boson universality comes back and the ω^2 term dominates over the susceptibility, consistent with our observation of the bare boson susceptibility. We also note that because the frequency dependence here is polluted by the IR irrelevant ω^2 contributions, whose contribution is about 10% at $\omega\sim0.25$, this frequency exponent has a lower accuracy, in comparison with the momentum dependence shown in Fig. 5*A*. Although the data are consistent with dynamical exponent $z=2$, small corrections in the form of an anomalous dimension in the dynamical exponent as predicted in ref. 26 cannot be excluded.

In the absence of fermions, $\chi^{-1}(0,h_c,|\mathbf{q}|,0)\propto|\mathbf{q}|^{1.96}$ [$(2+1)$D Ising]. According to the Hertz–Millis theory, this exponent should increase from 1.96 to 2 in the presence of fermions $\chi^{-1}(0,h_c,\mathbf{q},0)\propto|\mathbf{q}|^2$. Such an increase is indeed observed in the triangular lattice model ($2\mathbf{Q}\neq\Gamma$) (40). However, it is remarkable that for the square lattice model ($2\mathbf{Q}=\Gamma$), exactly the opposite was observed. Instead of increasing, this power actually decreases from 1.96 to 1.75, $\chi^{-1}(0,h_c,\mathbf{q},0)\propto|\mathbf{q}|^{1.75}$. Such a significant contrast is beyond numerical error, and it indicates that QCPs with $2\mathbf{Q}\neq\Gamma$ and $2\mathbf{Q}=\Gamma$ belong to totally different universality classes, which is one of the key observations in our study.

This difference can be understood in the following way. Between $2\mathbf{Q}=\Gamma$ and $2\mathbf{Q}\neq\Gamma$, the constraints that the momentum conservation law enforces are different. As shown in ref. 23, the QCPs with $2\mathbf{Q}=\Gamma$ deviate from the Hertz–Millis theory already at the level of 4-boson vertex correction, as shown in Fig. 6*A*. For $2\mathbf{Q}=\Gamma$, this 4-boson vertex shows 2 topologically different bosonic self-energy diagrams, Fig. 6 *B* and *C*, and in particular the diagram shown in Fig. 6*C* results in logarithmic corrections and is responsible for the breakdown of the Hertz–Millis scaling. However, for $2\mathbf{Q}\neq\Gamma$ (e.g., in the triangular lattice model, we have $3\mathbf{Q}=\Gamma$ instead), this crucial diagram is prohibited by the momentum conservation law, and thus, at least within the same level of approximation, deviations from the Hertz–Millis picture are not expected. Further investigations, both analytical and numerical, are needed to better understand the role of this subtle difference, as well as the RG flows in other cases like $3\mathbf{Q}=\Gamma$, etc.

Comparison with RG Analysis. On the theory side, perturbative renormalization group calculation has been performed for Heisenberg AFM-QCPs with SU(2) symmetry (23, 26), while the same study for Ising spins has not yet been carefully analyzed to our best knowledge. However, because some of the key features in the RG analysis are insensitive to the spin symmetry (23, 26), many qualitative results will hold and thus here we compare our numerical results with existing theoretical predictions for Heisenberg AFM-QCPs, but it must also be emphasized that agreement at the quantitative level is not expected here because of this difference in symmetry.

In the perturbative renormalization group calculation (23, 26), the anomalous dimension depends on the angle between the hotspot Fermi velocity and the order wavevector $\vec{Q}$. As shown below, for our model, this angle is close to $45°$. At this

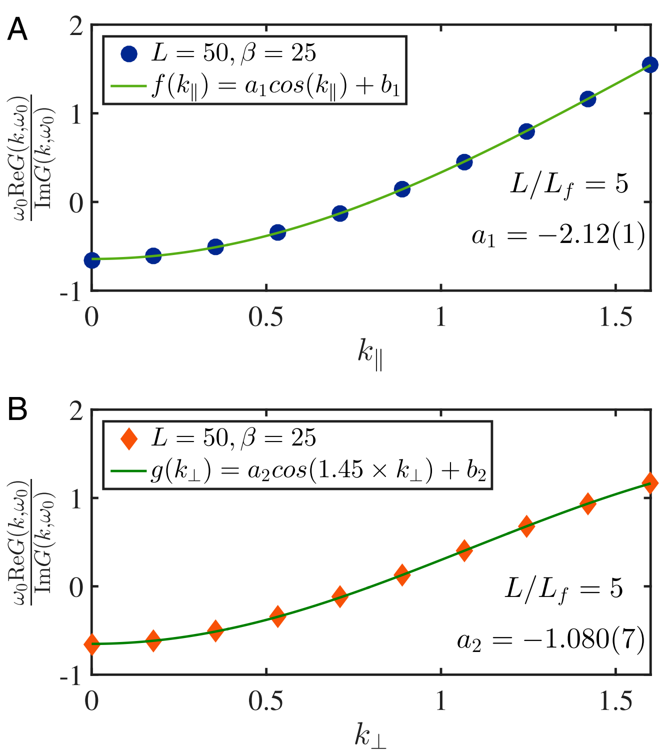

Fig. 7. (*A* and *B*) $\frac{\omega_0\mathrm{Re}G(k,\omega_0)}{\mathrm{Im}G(k,\omega_0)}$ variation (*A*) along the $Q=(\pi,\pi)$ direction $k_\parallel$ and (*B*) perpendicular to the $Q=(\pi,\pi)$ direction $k_\perp$ at the K'_3 hotspot mesh shown in Fig. 1. We use the simple trigonometric function $f(k_\parallel)$ and $g(k_\perp)$ to fit the data in *A* and *B*.

Table 1. The Fermi velocity v_F at the hotspot in the K_3' hotspot mesh obtained from $\frac{\omega_0 \mathrm{Re}G(k,\omega_0)}{\mathrm{Im}G(k,\omega_0)}$ data shown in Fig. 7 and the Fermi velocity in the free-fermion case

Hotspots location	k_x	k_y
	2.5800	0.5615
v_F at hotspots	$v_\parallel$	$v_\perp$
Near QCP	1.523(8)	1.435(8)
Free fermion	1.506	1.468

angle, the RG prediction for the anomalous dimension is $\eta = 1/N_{h.s.}$, where $N_{h.s.}$ is the number of hotspots (23, 26). In our model, $N_{h.s.} = 16$, and thus the RG predicted value is $\eta = 1/16$. However, as shown above, although we observed the same qualitative behavior, the value of η that we observed is close to $2/N_{h.s.}$ instead. Whether this quantitative disagreement is due to the symmetry difference (Heisenberg vs. Ising) or some other contributions is an interesting open question.

In addition, the RG analysis also predicts that near the QCP the Fermi surface at hotspots will rotate toward nesting (23). This rotation of the Fermi surface will further increase the anomalous dimension and can even renormalize the value of the dynamic critical exponent z (23, 26). As is shown below, our study indeed observed this Fermi surface rotation near the QCP. However, because this RG flow is very slow, our hotspot Fermi surface rotated only by about 0.5° in our simulation before being stopped by a cutoff. For such a small rotation, the resulting increase of the anomalous dimension and the change in the dynamic critical exponent are too weak to be observed.

We calculate the Fermi velocity v_F as

$$\mathbf{v}_F = \frac{\partial}{\partial_{\mathbf{k}}} \frac{\omega_0 \mathrm{Re}G(k,\omega_0)}{\mathrm{Im}G(k,\omega_0)}\bigg|_{\mathbf{k}=\mathbf{k}_F}, \qquad [12]$$

where $\omega_0 = \pi/\beta$. To accurately compute the derivative, we first use simple functions to fit the discrete data points of $\frac{\omega_0 \mathrm{Re}G(k,\omega_0)}{\mathrm{Im}G(k,\omega_0)}$ vs. $\mathbf{k}$ as shown in Fig. 7. Then, we compute the derivative for the fitting function to obtain the Fermi velocity, which is recorded in Table 1. $v_\parallel$ and $v_\perp$ are the 2 components of the Fermi velocity at a hotspot parallel and perpendicular to $\mathbf{Q}$, respectively. In Table 1, we showed both the noninteracting Fermi velocity (bare values) and the Fermi velocity measured at the QCP (renormalized values).

According to the RG analysis (23), $v_\parallel$ and $v_\perp$ will flow to infinity and 0, respectively, but at the same time their product $v_\parallel \times v_\perp$ will remain a constant. In a numerical simulation, this RG flow will be stopped by numerical cutoffs, e.g., finite-size effects. Because this RG flow is marginal at the tree level, the flow is expected to be very slow (logarithmic) and thus our observed renormalized value will not differ dramatically from the bare ones. As can be seen from Table 1, this is indeed what we observed. The renormalized value of $v_\parallel$ ($v_\perp$) is slightly larger (smaller) than its bare value, and the product of $v_\parallel$ and $v_\perp$ remains largely a constant (2.210 for the bare values and 2.186 for the renormalized ones), as the RG theory predicts. It is worthwhile to highlight here that although changes in $v_\parallel$ and $v_\perp$ are small, they are beyond numerical error as shown in Table 1, and theoretically, these small changes are consistent with the slow RG flow predicted by theory.

Discussion

If we compare the AFM-QCPs with $2\mathbf{Q} \neq \Gamma$ and $2\mathbf{Q} = \Gamma$, QMC studies indicate that they belong to 2 different universality classes, in contrast to the Hertz–Millis prediction, which does not rely on the value of $\mathbf{Q}$. This observation supports the $1/N_{h.s.}$ expansion and RG analysis discussed in ref. 23.

In the study of criticality and anomalous critical scalings, the comparison between theory and numerical results plays a vital role. For QCPs in itinerant fermion systems, although non–mean-field scaling beyond the Hertz–Millis theory has been predicted in theory and observed in QMC simulations, it has been a long-standing challenge to reconcile numerical and theoretical results. Our study offers a solid example where an agreement between theory and numerical simulations starts to emerge, which is 1 first step toward a full understanding about itinerant QCPs (32). In particular, to pinpoint the exact value of the frequency exponent and to probe the predicted anomalous dynamical critical exponents (26, 28, 29), lower temperature and frequency range need to be explored. As pointed out in ref. 31, future works along this line are highly desirable and are actively being pursued by us (32).

At the technical level, a combination of DQMC and EQMC methodologies in this work shows a very promising direction in the numerical investigations of itinerant QCPs. Besides the consistency check in ref. 41 for triangular lattice AFM-QCP, the square lattice AFM-QCP investigated here provides the second example of the consistency in DQMC and EQMC in terms of revealing critical properties. Such consistency suggests another pathway for future studies about quantum criticality in fermionic systems, in that one can use DQMC on small systems to provide benchmark results and use EQMC to reveal IR physics at the thermodynamic limit.

ACKNOWLEDGMENTS. We acknowledge valuable discussions with Avraham Klein, Sung-Sik Lee, Yoni Schattner, Andrey Chubukov, Subir Sachdev, and Steven Kivelson on various subjects of itinerant quantum criticality. Z.H.L., G.P., and Z.Y.M. acknowledge funding from the Ministry of Science and Technology of China through the National Key Research and Development Program (2016YFA0300502); the Strategic Priority Research Program of the Chinese Academy of Sciences (XDB28000000); and the National Science Foundation of China under Grants 11421092, 11574359, and 11674370. X.Y.X. is thankful for the support of Hong Kong Research Grants Council through Grant C6026-16W. K.S. acknowledges support from the National Science Foundation under Grant EFRI-1741618 and the Alfred P. Sloan Foundation. We thank the Center for Quantum Simulation Sciences in the Institute of Physics, Chinese Academy of Sciences and the Tianhe-1A and Tianhe-II platforms at the National Supercomputer Centers in Tianjin and Guangzhou for their technical support and generous allocation of CPU time.

1. J. A. Hertz, Quantum critical phenomena. *Phys. Rev. B* **14**, 1165–1184 (1976).
2. A. J. Millis, Effect of a nonzero temperature on quantum critical points in itinerant fermion systems. *Phys. Rev. B* **48**, 7183–7196 (1993).
3. T. Moriya, *Spin Fluctuations in Itinerant Electron Magnetism* (Springer-Verlag, Berlin/Heidelberg, Germany, 1985).
4. G. R. Stewart, Non-Fermi-liquid behavior in *d*- and *f*-electron metals. *Rev. Mod. Phys.* **73**, 797–855 (2001).
5. A. V. Chubukov, C. Pépin, J. Rech, Instability of the quantum-critical point of itinerant ferromagnets. *Phys. Rev. Lett.* **92**, 147003 (2004).
6. D. Belitz, T. R. Kirkpatrick, T. Vojta, How generic scale invariance influences quantum and classical phase transitions. *Rev. Mod. Phys.* **77**, 579–632 (2005).
7. H. v. Löhneysen, A. Rosch, M. Vojta, P. Wölfle, Fermi-liquid instabilities at magnetic quantum phase transitions. *Rev. Mod. Phys.* **79**, 1015–1075 (2007).
8. A. V. Chubukov, D. L. Maslov, Spin conservation and Fermi liquid near a ferromagnetic quantum critical point. *Phys. Rev. Lett.* **103**, 216401 (2009).
9. W. Metzner, D. Rohe, S. Andergassen, Soft Fermi surfaces and breakdown of Fermi-liquid behavior. *Phys. Rev. Lett.* **91**, 066402 (2003).
10. T. Senthil, Critical Fermi surfaces and non-Fermi liquid metals. *Phys. Rev. B* **78**, 035103 (2008).
11. T. Holder, W. Metzner, Anomalous dynamical scaling from nematic and u(1) gauge field fluctuations in two-dimensional metals. *Phys. Rev. B* **92**, 041112 (2015).
12. M. A. Metlitski, D. F. Mross, S. Sachdev, T. Senthil, Cooper pairing in non-Fermi liquids. *Phys. Rev. B* **91**, 115111 (2015).
13. X. Y. Xu, K. Sun, Y. Schattner, E. Berg, Z. Y. Meng, Non-Fermi liquid at $(2+1)$D ferromagnetic quantum critical point. *Phys. Rev. X* **7**, 031058 (2017).
14. J. Custers *et al.*, The break-up of heavy electrons at a quantum critical point. *Nature* **424**, 524–527 (2003).
15. A. Steppke *et al.*, Ferromagnetic quantum critical point in the heavy-fermion metal YbNi4($P_{1-x}As_x$)2. *Science* **339**, 933–936 (2013).

16. W. Zhang *et al.*, Effect of nematic order on the low-energy spin fluctuations in detwinned bafe$_{1.935}$ni$_{0.065}$as$_2$. *Phys. Rev. Lett.* **117**, 227003 (2016).
17. Z. Liu *et al.*, Nematic quantum critical fluctuations in bafe$_{2-x}$ni$_x$as$_2$. *Phys. Rev. Lett.* **117**, 157002 (2016).
18. Y. Gu *et al.*, Unified phase diagram for iron-based superconductors. *Phys. Rev. Lett.* **119**, 157001 (2017).
19. W. Wu *et al.*, Superconductivity in the vicinity of antiferromagnetic order in CrAs. *Nat. Commun.* **5**, 5508 (2014).
20. J. G. Cheng *et al.*, Pressure induced superconductivity on the border of magnetic order in MnP. *Phys. Rev. Lett.* **114**, 117001 (2015).
21. M. Matsuda *et al.*, Evolution of magnetic double helix and quantum criticality near a dome of superconductivity in CrAs. *Phys. Rev. X* **8**, 031017 (2018).
22. J. Cheng, J. Luo, Pressure-induced superconductivity in CrAs and MnP. *J. Phys. Condens. Matter* **29**, 383003 (2017).
23. A. Abanov, A. V. Chubukov, J. Schmalian, Quantum-critical theory of the spin-fermion model and its application to cuprates: Normal state analysis. *Adv. Phys.* **52**, 119–218 (2003).
24. A. Abanov, A. Chubukov, Anomalous scaling at the quantum critical point in itinerant antiferromagnets. *Phys. Rev. Lett.* **93**, 255702 (2004).
25. M. A. Metlitski, S. Sachdev, Quantum phase transitions of metals in two spatial dimensions. I. Ising-nematic order. *Phys. Rev. B* **82**, 075127 (2010).
26. M. A. Metlitski, S. Sachdev, Quantum phase transitions of metals in two spatial dimensions. II. Spin density wave order. *Phys. Rev. B* **82**, 075128 (2010).
27. S. Sur, S. S. Lee, Anisotropic non-Fermi liquids. *Phys. Rev. B* **94**, 195135 (2016).
28. A. Schlief, P. Lunts, S. S. Lee, Exact critical exponents for the antiferromagnetic quantum critical metal in two dimensions. *Phys. Rev. X* **7**, 021010 (2017).
29. S. S. Lee, Recent developments in non-Fermi liquid theory. *Annu. Rev. Condens. Matter Phys.* **9**, 227–244 (2018).
30. A. Schlief, P. Lunts, S. S. Lee (2018) Noncommutativity between the low-energy limit and integer dimension limits in the ϵ-expansion: A case study of the antiferromagnetic quantum critical metal. arXiv:1805.05252 (19 July 2018).
31. A. Chubukov, Solving metallic quantum criticality in a casino. *J. Club Condens. Matter Phys.*, 201802 (2018).
32. X. Y. Xu *et al.*, Revealing fermionic quantum criticality from new Monte Carlo techniques. arXiv:1904.07355 (15 April 2019).
33. Y. Schattner, S. Lederer, S. A. Kivelson, E. Berg, Ising nematic quantum critical point in a metal: A Monte Carlo study. *Phys. Rev. X* **6**, 031028 (2016).
34. S. Lederer, Y. Schattner, E. Berg, S. A. Kivelson, Superconductivity and non-Fermi liquid behavior near a nematic quantum critical point. *Proc. Natl. Acad. Sci. U.S.A.* **114**, 4905–4910 (2017).
35. Z. X. Li, F. Wang, H. Yao, D. H. Lee, The nature of effective interaction in cuprate superconductors: A sign-problem-free quantum Monte-Carlo study. ArXiv:1512.04541 (14 December 2015).
36. E. Berg, M. A. Metlitski, S. Sachdev, Sign-problem–free quantum Monte Carlo of the onset of antiferromagnetism in metals. *Science* **338**, 1606–1609 (2012).
37. Z. X. Li, F. Wang, H. Yao, D. H. Lee, What makes the Tc of monolayer FeSe on SrTiO3 so high: A sign-problem-free quantum Monte Carlo study. *Sci. Bull.* **61**, 925–930 (2016).
38. Y. Schattner, M. H. Gerlach, S. Trebst, E. Berg, Competing orders in a nearly antiferromagnetic metal. *Phys. Rev. Lett.* **117**, 097002 (2016).
39. M. H. Gerlach, Y. Schattner, E. Berg, S. Trebst, Quantum critical properties of a metallic spin-density-wave transition. *Phys. Rev. B* **95**, 035124 (2017).
40. Z. H. Liu, X. Y. Xu, Y. Qi, K. Sun, Z. Y. Meng, Itinerant quantum critical point with frustration and a non-Fermi liquid. *Phys. Rev. B* **98**, 045116 (2018).
41. Z. H. Liu, X. Y. Xu, Y. Qi, K. Sun, Z. Y. Meng, Elective-momentum ultrasize quantum Monte Carlo method. *Phys. Rev. B* **99**, 085114 (2019).
42. X. Y. Xu, K. S. D. Beach, K. Sun, F. F. Assaad, Z. Y. Meng, Topological phase transitions with SO(4) symmetry in (2+1)d interacting Dirac fermions. *Phys. Rev. B* **95**, 085110 (2017).
43. F. F. Assaad, T. Grover, Simple fermionic model of deconfined phases and phase transitions. *Phys. Rev. X* **6**, 041049 (2016).
44. S. Gazit, M. Randeria, A. Vishwanath, Emergent Dirac fermions and broken symmetries in confined and deconfined phases of z2 gauge theories. *Nat. Phys.* **13**, 484–490 (2017).
45. Y. Y. He *et al.*, Dynamical generation of topological masses in Dirac fermions. *Phys. Rev. B* **97**, 081110 (2018).
46. X. Y. Xu *et al.*, Monte Carlo study of lattice compact quantum electrodynamics with fermionic matter: The parent state of quantum phases. *Phys. Rev. X* **9**, 021022 (2019).
47. C. Chen, X. Y. Xu, Y. Qi, Z. Y. Meng, Metals' awkward cousin is found. arXiv:1904.12872 (29 April 2019).
48. J. Liu, Y. Qi, Z. Y. Meng, L. Fu, Self-learning Monte Carlo method. *Phys. Rev. B* **95**, 041101 (2017).
49. J. Liu, H. Shen, Y. Qi, Z. Y. Meng, L. Fu, Self-learning Monte Carlo method and cumulative update in fermion systems. *Phys. Rev. B* **95**, 241104 (2017).
50. X. Y. Xu, Y. Qi, J. Liu, L. Fu, Z. Y. Meng, Self-learning quantum Monte Carlo method in interacting fermion systems. *Phys. Rev. B* **96**, 041119 (2017).
51. Y. Nagai, H. Shen, Y. Qi, J. Liu, L. Fu, Self-learning Monte Carlo method: Continuous-time algorithm. *Phys. Rev. B* **96**, 161102 (2017).
52. H. Shen, J. Liu, L. Fu, Self-learning Monte Carlo with deep neural networks. *Phys. Rev. B* **97**, 205140 (2018).
53. C. Chen *et al.*, Symmetry-enforced self-learning Monte Carlo method applied to the Holstein model. *Phys. Rev. B* **98**, 041102 (2018).
54. C. Chen, X. Y. Xu, Z. Y. Meng, M. Hohenadler, Charge-density-wave transitions of Dirac fermions coupled to phonons. *Phys. Rev. Lett.* **122**, 077601 (2019).
55. K. Sun, B. M. Fregoso, M. J. Lawler, E. Fradkin, Fluctuating stripes in strongly correlated electron systems and the nematic-smectic quantum phase transition. *Phys. Rev. B* **78**, 085124 (2008).
56. E. Berg, S. Lederer, Y. Schattner, S. Trebst, Monte Carlo studies of quantum critical metals. *Annu. Rev. Condens. Matter Phys.* **10**, 63–84 (2019).
57. H. W. J. Blöte, Y. Deng, Cluster Monte Carlo simulation of the transverse Ising model. *Phys. Rev. E* **66**, 066110 (2002).
58. S. Hesselmann, S. Wessel, Thermal Ising transitions in the vicinity of two-dimensional quantum critical points. *Phys. Rev. B* **93**, 155157 (2016).
59. D. Chowdhury, S. Sachdev, Density-wave instabilities of fractionalized Fermi liquids. *Phys. Rev. B* **90**, 245136 (2014).
60. Y. C. Wang, Y. Qi, S. Chen, Z. Y. Meng, Caution on emergent continuous symmetry: A Monte Carlo investigation of the transverse-field frustrated Ising model on the triangular and honeycomb lattices. *Phys. Rev. B* **96**, 115160 (2017).
61. U. Wolff, Collective Monte Carlo updating for spin systems. *Phys. Rev. Lett.* **62**, 361–364 (1989).
62. R. H. Swendsen, J. S. Wang, Nonuniversal critical dynamics in Monte Carlo simulations. *Phys. Rev. Lett.* **58**, 86–88 (1987).
63. R. Blankenbecler, D. J. Scalapino, R. L. Sugar, Monte Carlo calculations of coupled boson-fermion systems. I. *Phys. Rev. D* **24**, 2278–2286 (1981).
64. J. E. Hirsch, Discrete Hubbard-Stratonovich transformation for fermion lattice models. *Phys. Rev. B* **28**, 4059–4061 (1983).
65. F. Assaad, H. Evertz, "World-line and determinantal quantum Monte Carlo methods for spins, phonons and electrons" in *Computational Many-Particle Physics*, Lecture Notes in Physics, H. Fehske, R. Schneider, A. Weisse, Eds. (Springer, Berlin/Heidelberg, Germany, 2008), vol. 739, pp. 277–356.
66. M. A. Metlitski, S. Sachdev, Instabilities near the onset of spin density wave order in metals. *New J. Phys.* **12**, 105007 (2010).